SCIENCE CHINA
Physics, Mechanics & Astronomy

•**Article**•

March 2022 Vol. 65 No. 3: 237011
https://doi.org/10.1007/s11433-021-1820-4

Electrically driven motion, destruction, and chirality change of polar vortices in oxide superlattices

Pan Chen[1,2†], Congbing Tan[3†], Zhexin Jiang[4,10†], Peng Gao[2,5*], Yuanwei Sun[2], Lifen Wang[1],
Xiaomei Li[1], Ruixue Zhu[2], Lei Liao[1,6], Xu Hou[4], Ke Qu[2], Ning Li[2], Xiaomin Li[1], Zhi Xu[1,7],
Kaihui Liu[5,8], Wenlong Wang[1,7], Jinbin Wang[9], Xiaoping Ouyang[9], Xiangli Zhong[9*],
Jie Wang[4,10*], and Xuedong Bai[1,6,7*]

[1] *Beijing National Laboratory for Condensed Matter Physics, Institute of Physics, Chinese Academy of Sciences, Beijing 100190, China;*
[2] *International Center for Quantum Materials, Electron Microscopy Laboratory, School of Physics, Peking University, Beijing 100871, China;*
[3] *Hunan Provincial Key Laboratory of Intelligent Sensors and Advanced Sensor Materials, School of Physics and Electronics, Hunan University of Science and Technology, Xiangtan 411201, China;*
[4] *Department of Engineering Mechanics, Zhejiang University, Hangzhou 310027, China;*
[5] *Collaborative Innovation Center of Quantum Matter, Beijing 100871, China;*
[6] *School of Physical Sciences, University of Chinese Academy of Sciences, Beijing 100190, China;*
[7] *Songshan Lake Materials Laboratory, Dongguan 523808, China;*
[8] *State Key Laboratory for Artificial Microstructure & Mesoscopic Physics, School of Physics, Peking University, Beijing 100871, China;*
[9] *School of Materials Science and Engineering, Xiangtan University, Xiangtan 411105, China;*
[10] *Key Laboratory of Soft Machines and Smart Devices of Zhejiang Province, Zhejiang University, Hangzhou 310027, China*

Received November 3, 2021; accepted November 23, 2021; published online January 17, 2022

Topological polar vortices, which are electric analogs of magnetic objects, present great potential in applications of future nanoelectronics because of their nanometer size, anomalous dielectric response, and chirality. To enable the functionalities, it is prerequisite to manipulate the polar states and chirality by using external stimuli. Here, we probe the evolutions of polar state and chirality evolutions of topological polar vortices in $PbTiO_3/SrTiO_3$ superlattices under an electric field by using atomically resolved *in situ* scanning transmission electron microscopy and phase-field simulations. We find that, under electric field, the chiral vortex cores can be moved laterally to form close-pair structures, transform into *a*/c domain stripes, and finally become a nonchiral c-domain. Such transition is reversible and spontaneous after bias removal. Interestingly, during switching and back-switching events, the vortex rotation can be changed, offering a potential strategy to manipulate vortex chirality. The revealed dynamic behavior of individual polar vortices at the atomic scale provides fundamentals for future device applications.

chirality, polar vortex, ferroelectrics, *in situ* transmission electron microscopy, phase-field simulations

PACS number(s): 68.37.Lp, 73.21.cd, 77.80.Dj, 77.84.-s

Citation: P. Chen, C. Tan, Z. Jiang, P. Gao, Y. Sun, L. Wang, X. Li, R. Zhu, L. Liao, X. Hou, K. Qu, N. Li, X. Li, Z. Xu, K. Liu, W. Wang, J. Wang, X. Ouyang, X. Zhong, J. Wang, and X. Bai, Electrically driven motion, destruction, and chirality change of polar vortices in oxide superlattices, Sci. China-Phys. Mech. Astron. **65**, 237011 (2022), https://doi.org/10.1007/s11433-021-1820-4

---

*Corresponding authors (Peng Gao, email: p-gao@pku.edu.cn; Xiangli Zhong, email: xlzhong@xtu.edu.cn; Jie Wang, email: jw@zju.edu.cn; Xuedong Bai, email: xdbai@iphy.ac.cn)
†These authors contributed equally to this work.

1 Introduction

Polar vortex, a topological structure with electric dipoles continuously rotating around a stable core, exhibits new emergent ordering and properties [1-3], thus attracting extensive research attention [4-7]. Such vortices have been theoretically predicted and experimentally realized in low-dimensional ferroelectrics [8-10]. Recently, the vortex array has been discovered in $(PbTiO_3)_n/(SrTiO_3)_m$ superlattices (PTO/STO, where n and m are the number of unit cells for PTO and STO, respectively) with alternating clockwise and counterclockwise rotations of electric dipoles [1]. The vortex is an ideal storage unit for high-density memory applications because of its long-range ordering within the superlattices and nanometer size [2,4,11]. On the other hand, the PTO/STO superlattices with vortex arrays show anomalous dielectric behavior or negative capacitance, which has great potential for semiconducting electronics to overcome Boltzmann's tyranny [4]. Moreover, these vortices carry chirality [12,13], providing a new order parameter for these complex oxides, thus enabling novel functionalities and devices.

In order to enable these applications of the polar vortex, it is prerequisite to manipulate the ferroelectric order parameters and/or vortex chirality. Theoretical investigations [14,15] have predicted the evolution path from the vortex to trivial ferroelectrics under an external electric field, i.e., clockwise and counterclockwise vortices melt to form *a*/c domains. Experimentally, Damodaran et al. [6] demonstrated the interconversion between the vortex and the ferroelectric a_1/a_2 domains under an electric field via atomic force microscopy. Using *in situ* transmission electron microscopy (TEM), Du et al. [16] showed a local transformation from the vortex into the dipole wave and the *c* domain by applying noncontact bias. They found that the transitioned states are sustained even with the removal of electric bias. Nelson et al. [17] have controversially found the vortex response to the applied electric field through a reversible transition to the *a*/*c* domain or *a*-domain, casting debate on the switching pathways that further hinder their potential applications. Aside from the electric field-driven phase transition, Chen et al. [18] observed that mechanical stress can cause similar phase transitions between the topological polar state and the trivial ferroelectric phase (i.e., *a*-domain).

By contrast, the chirality of polar vortices has been rarely explored because of the difficulties in characterization. The chirality of polar vortices is determined by both the rotation direction and the axial component of polarization along the vortex tube direction [12], and it can be used as a new parameter for future device applications. The switching of vortex rotation is predicted either by a curled electric field [19,20] or by deliberately designed nanostructures (such as notched nanodots, asymmetric nanorings, and void nanoplatelet) [21-23], which is impractical for applications because of the difficulties in controlling the distribution of electric fields or the fabrication of such complicated nanostructures. Thus, new possible strategies must be explored to control the rotation and the chirality of vortices by using regular electric fields.

Here, by using an atomically resolved *in situ* scanning transmission electron microscopy (STEM) method, we probe the dynamic evolutions of polar state and chirality in individual polar vortices in $PbTiO_3/SrTiO_3$ superlattices under an electric field. We find that the vortex core can move laterally when the external field gradually aligns electric dipoles along the out-of-plane direction. With increasing field strength, the topological polar vortices are broken and transformed into *a*/*c* domain, and then they become a mono nonchiral *c*-domain, which is in excellent agreement with phase-field simulations. Removal of the external electric field leads to spontaneous back switching to the original vortex array. In addition, the rotation of the chiral vortex can be changed during switching and back-switching events, enabling the manipulation of individual vortex chirality by using a simple external electric field. Our work reveals the reversible switching pathways of individual vortices at the atomic scale and demonstrates the ability to electrically tune the vortex rotation, which may open a new strategy to control the chirality and further utilize it as a new order parameter for novel device applications.

2 Materials and methods

2.1 Thin film growth

The bottom electrode layer of ~10 nm $SrRuO_3$ was grown on $(110)_o$-$DyScO_3$ substrates, followed by the growth of $(PbTiO_3)_n/(SrTiO_3)_n$ superlattice films by a pulsed laser deposition system (PVD-5000) using a KrF excimer laser (λ = 248 nm). During the growth of $SrRuO_3$, the substrate temperature was maintained at 690°C with an oxygen pressure of 80 mTorr and a laser energy of 390 mJ pulse^{-1}. When the substrate temperature was cooled down to 600°C, the n uc-thick $PbTiO_3$ and $SrTiO_3$ layers were alternately deposited at an oxygen pressure of 200 mTorr with a laser energy of 340 mJ pulse^{-1}. The thicknesses of the $SrRuO_3$, $PbTiO_3$, and $SrTiO_3$ layers were held by controlling the growth time under a pulse repetition rate of 10 Hz. Ceramic target $Pb_{1.1}TiO_3$ with a 10 mol% excessive amount of lead was used to compensate for the evaporation loss of Pb during the growth of the $PbTiO_3$ layer. After the growth of the 15- $(PbTiO_3)_n/(SrTiO_3)_n$ cycles, the samples were cooled down to room temperature at 10°C/min in 200 mTorr oxygen pressure.

2.2 Sample preparation and *in situ* (S)TEM characterization

TEM cross-sectional samples were polished to approximately 30 μm by using conventional mechanical methods and then transferred to ion-beam milling in a Gatan PIPS 695 system with an acceleration voltage of 3 kV for quick milling followed by the final 0.1 kV to reduce damage. *In situ* TEM experiments were carried out using a customized holder from ZepTools Technology Company on JEOL ARM 300F to get atomic resolution even under an electric field because of the good stability of the holder. Electric bias was applied to the PTO/STO films, with the scanning tungsten tip serving as the top electrode and the conductive SRO layer serving as the bottom electrode. The *in situ* experiment was carried out in TEM mode for the dark-field and electron diffraction. Dark-field images were acquired under two-beam conditions with $(002)_{pc}$ ("pc" denotes the pseudocubic indices) selected for the optimal image condition. The atomic HAADF-STEM images were acquired under an electric field with a dwell time of 4 μs per pixel. In STEM mode, whether the electric field was applied to the samples can be judged from the current values. Markers were created for calibration by focusing the electron probe on a specific location for a few minutes.

2.3 Phase-field modeling

The details of phase-field methods are provided in Supporting Information online.

3 Results and discussion

$(PTO)_n/(STO)_m$ thin films were synthesized on $(001)_{pc}$ $DyScO_3$ substrate with $SrRuO_3$ as the bottom electrode through pulsed laser deposition (Methods). Figure 1(a) and (b) are low-magnification dark-field images of the plane view and cross-section samples, respectively. The stripes in Figure 1(a) are vortex tubes (Figure S1, Supporting Information online), and the alternating bright and dark contrasts in dark-field TEM image (Figure 1(b)) correspond to the clockwise and counterclockwise vortex arrays that exhibit long-range ordering, wherein the out-of-plane **g**-vector $(002)_{pc}$ is selected to distinguish $P_{[001]}\uparrow$ and $P_{[001]}\downarrow$ components. The phase-field simulations in Figure 1(c) show the

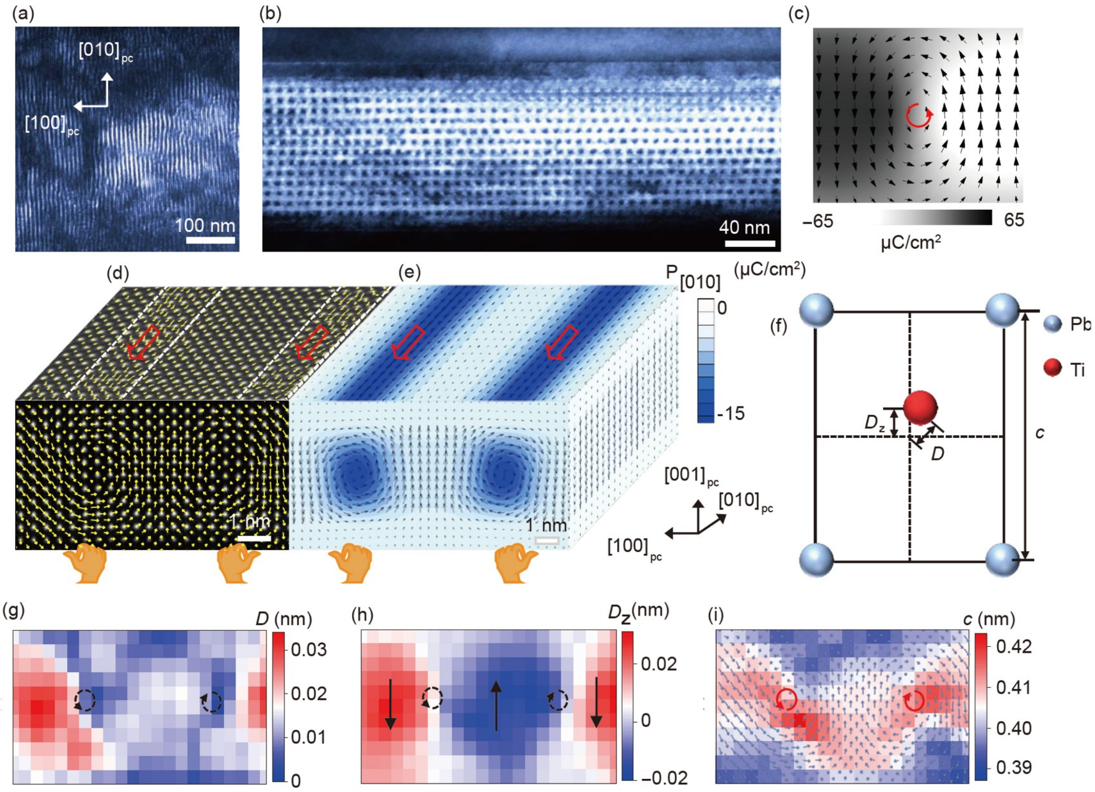

Figure 1 (Color online) Characterization of vortex chirality in $PbTiO_3/SrTiO_3$ superlattices. (a) Plane view dark-field image, indicating the long-range in-plane ordering. (b) Cross-sectional dark-field image under two-beam conditions (vector $\mathbf{g} = 002_{pc}$, pc denotes pseudocubic indices) with alternative bright and dark contrasts corresponding to the clockwise and counterclockwise vortex pairs. (c) Distribution of out-of-plane polarization simulated by phase-field simulations with the bright and dark contrast resembling the contrast of the dark-field image. The vortex core is located in the boundary of the bright and dark areas. (d) Atomically resolved HAADF-STEM image with the yellow displacement vectors exhibiting a vortex pair. The image overlaid above is a HAADF-STEM image showing a parallel axial polarization for a vortex pair. (e) The configuration of the vortex reproduced by phase-field simulation, in good agreement with experimental results. The chirality of the vortex is determined by the vortex rotation and axial polarization. Thus, an opposite chirality (indicated by the orange hand label) is derived by curling the fingers along the rotation and thumbs pointing to the direction of axial polarization. (f) Schematic of the perovskite $PbTiO_3$ structure with D_z, D, and c representing the [001] component of displacement, total displacement, and c lattice constant, respectively. (g)-(i) Total polarization, out-of-plane polarization distribution, and out-of-plane lattice mapping of the vortex in (d), respectively. The core positions and rotation directions can be identified from these maps.

distribution of polarization vectors corresponding to the contrast in the dark-field TEM image [24]. Thus, the core position of the vortex can be located in the boundary between the dark and bright areas from the dark-field TEM image. The PTO/STO superlattice film shows sharp interfaces confirmed by the atomically resolved EDS mapping in Figure S2. Dipole configuration can be evidenced by calculating the offset of Pb/Sr and Ti sublattices on the basis of the atomically resolved HAADF-STEM image shown in Figure 1(d) for the cross-sectional view and plane view, from which the adjacent clockwise and counterclockwise vortices have opposite rotations but the same axial component, leading to opposite chirality. Phase-field simulations reproduce the same polarization configuration shown in Figure 1(e). The polarization is much smaller along the tube direction ($[010]_{pc}$) than along the other directions ($[001]_{pc}$) (Figure S3). Such small values are difficult to extract from the quantitative analysis of electron microscopy images [25], which explains why previous electron microscopy studies rarely discussed chirality [16,18,26]. It is even harder to detect the axial polarization component for *in situ* TEM experiments that generally suffer relatively large vibrations and instabilities due to the introduction of the contacting probe and applied fields. Thus, we performed the *in situ* experiments from the cross-sectional view operated under low-magnification dark-field and atomically resolved HAADF modes to track the evolution of the rotation direction. Furthermore, as illustrated in Figure 1(f), the displacement maps (Figure 1(g) and (h)) and out-of-plane lattice constant (Figure 1(i)) can be extracted from the atomically resolved HAADF image (Figure 1(d)). For each unit cell, the core positions and possible domain wall positions can be located, and the rotation direction can be identified from these maps [27]. In particular, the vortex core lies in the boundary of the upward and downward out-of-plane displacement regions (Figure 1(g) and (h)) similar to the dark-field TEM image, and it can also be reflected in the lattice mapping with a much better signal-to-noise ratio (Figure 1(i)) because the polarization is highly correlated with the lattice. Therefore, the evolution of rotation direction for each vortex during *in situ* biasing can be reliably tracked by multiple parameters (e.g., dark-field TEM image, out-of-plane polarization mapping, and lattice c mapping) in decent atomically resolved images.

An electric field is applied to the vortex between the probe and the SRO bottom electrode, as illustrated in Figure S4(a). With the bias exceeding 6 V, the alternating bright and dark contrasts become uniform underneath the probe (Figure 2(a)), indicating realignment of the electric dipoles in the vortex (i.e., polarization switching). The transition is initiated at the contacting point between the surface and the probe, where the electric field is larger because of the tip geometry electrode (Figure S4(b) and (c)). Thus, the barrier for switching is first to overcome. The fully switched region with uniform contrast highlighted by the red dashed outlines is the c-domain, as evidenced by the *in situ* electron diffraction experiment in Figure S5. Close inspection (Figure 2(b)) reveals that surrounding the fully switched region is an intermediated phase zone where the pristine dark dotted contrast becomes tilted stripes, which is a feature of a/c domains. An increase in bias leads to the growth of the fully switched regions, whereas removal of the bias results in spontaneous back switching to form the vortex array, indicating that the topological polar vortex is the most stable state. The spontaneous recovery is consistent with mechanical [18] and temperature [6] driven switching, which is in sharp contrast with the electric field-induced nonrecovery switching behavior [16,28] and different with the case of mixed phases of the vortex and the a-domain [6], in which back switching can only be driven by an electric field with the opposite direction.

Application of a negative bias also results in a transition

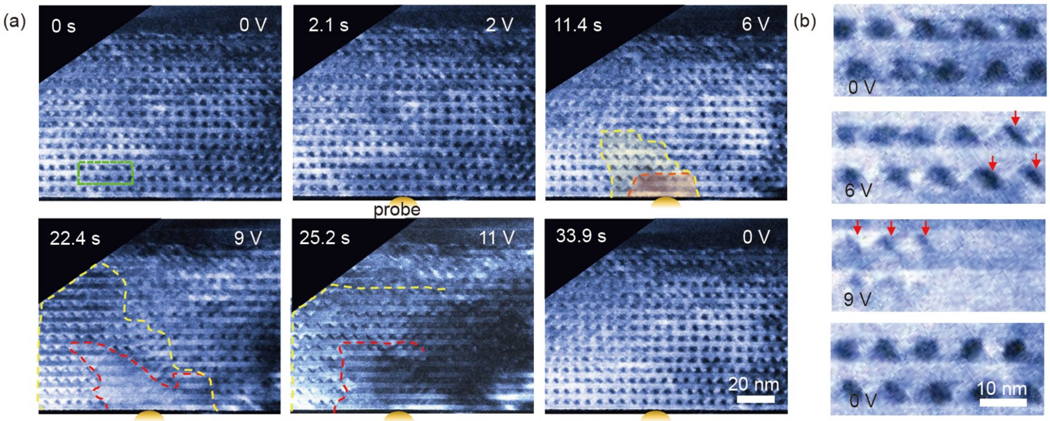

Figure 2 (Color online) Electrically driven transition of the polar vortex. (a) Consecutive TEM dark-field images showing a bias-induced transition from vortices to regular ferroelectric states. The red outline denotes the switched region of the c-domain, and the yellow dashed outline highlights the region of the intermediate phase. At 25.2 s, the outlines are not clear enough to be labeled in the right-side region. (b) Enlarged view of the vortex transition from the selected region (green rectangle) in (a). The arrows indicating the tilted stripes are the intermediate phase with striped a/c domains.

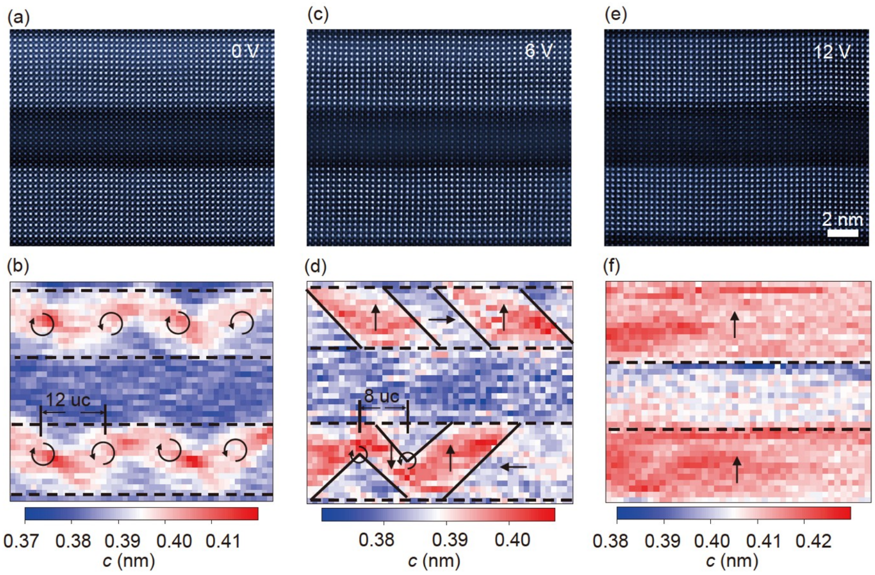

Figure 3 (Color online) Unit-cell scale mapping of the lattice constant. (a) HAADF-STEM image recorded from the pristine region with vortex array. (b) Corresponding lattice *c* mapping. Distance between the two cores is typically 12 unit cells. (c) HAADF-STEM image acquired from the region with the intermediate phase at 6 V and (d) the corresponding lattice *c* mapping. The sinusoidal wave changes into tilted stripes, indicating the formation of a/c domains. The c-domain with upward polarization is growing, and the c-domain with downward polarization is shrinking. The distance between the two highlighted cores is reduced to 8 unit cells. (e) HAADF-STEM image acquired from the fully switched region and (f) the corresponding lattice *c* mapping, confirming the final phase is c-domain with upward polarization.

between the polar vortex and the c-domain similar to that of the positive bias case, which is confirmed by time-series dark-field images (Figure S6) and electron diffraction patterns (Figure S7). The similarity of the vortex transition between positive and negative is indicative of a symmetric nature of energy with regard to the electric field, which is different from the regular ferroelectric switching behavior in a single film [29]. This demonstration of controllable polar states between topological polar texture and trivial ferroelectric phase by using an electric field provides the possibility for practical applications in nanoelectronics because of the nonlinear optical and piezoelectric responses between the vortex and the ferroelectric phase are different up to the order of magnitude [6].

In order to reveal the breaking dynamics for each vortex, the transition process is recorded at atomic resolution, and the polar feature is presented with the unit-cell mapping of the out-of-plane lattice. Application of a positive 6 V bias results in the formation of striped a/c domains, as shown in Figure 3(c) and (d), whereas the pristine unswitched region presents the sinusoidal feature in Figure 3(a) and (b) (see also Figures S8 and S9). Before the destruction of the vortex core, the electric field that favors upward polarization and suppresses the downward one is expected to drive the lateral movement of the vortex cores to adapt the expansion of the upward domain and the shrinkage of the downward domain, forming the close-pair structure [14]. With increasing the bias to 12 V, the electric dipoles are fully aligned along the out-of-plane direction to form a pure upward domain in Figure 3(e) and (f). The two-stage phase transition from the vortex to the c-domain with intermediate a/c striped domains was predicted through phase-field simulations [14]. Our experimental observations are different from the previously reported noncontact long electric pulse bias-induced switching event [16], in which the vortex would transform to a polar wave instead of a/c domain stripes. Such intermediate a/c domain stripes were also not observed from the mechanical switching of the vortex [18], indicating that the switching paths for these topological structures largely depend on external stimuli.

Aside from the ability to switch between topological texture and trivial ferroelectric states, chirality change for the vortex is also highly desirable [2] and prerequisite for applications. Current driven switching behaviors of magnetic skyrmions [30,31] have been realized because these topological objects are arising from the Dzyaloshinskii-Moriya [32] interaction and thus are not easily annihilated under an electric field. However, here the polar vortices favor a transition behavior of breaking the topological structure because they result from a competitive balance of extrinsic elastic, gradient, and electrostatic energy. Hence, such a balance is perturbed by an external electric field, causing the realignment of the polarization in the vortex to reduce electrostatic energy, leaving the direct manipulation of polar vortex chirality via a simple electric field extremely challenging [15,19-21].

We find that the vortex rotation can be switched during switching and back-switching events. Figure 4(a) and (d) are

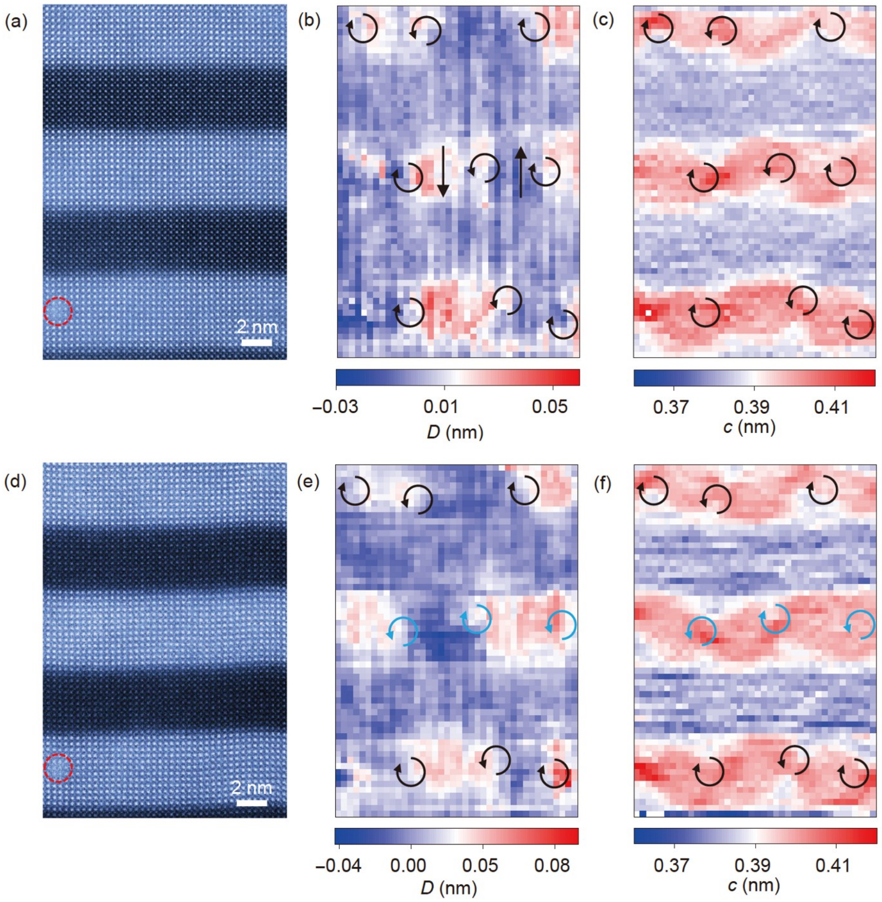

Figure 4 (Color online) Vortex rotation reversal. (a) HAADF-STEM image of the pristine vortex with a mark (denoted by the red circle) deliberately made by the focused electron beam. (b), (c) Corresponding out-of-plane displacement (denoted as *D*) and *c* lattice mapping of the vortex array. (d) HAADF-STEM image and (e), (f) corresponding out-of-plane displacement and *c* lattice mapping after removal of bias. Positions of vortex cores and rotation direction can be determined by the out-of-plane displacement mapping, although the noise is relatively large because of the larger vibration of *in situ* environments. While the positions of the vortex in the upper and bottom PTO layers maintain unaltered, the vortex in the middle PTO layer shows a rotation reversal.

the atomically resolved HAADF-STEM images acquired before and after electric field application for the same region that is tracked by a deliberately made mark (red circle) using an electron beam (Methods). The core position and rotation direction of the clockwise and counterclockwise vortices are labeled from the out-of-plane displacement distribution (Figure 4(b) and (e)) [27] and out-of-plane lattice mapping (Figure 4(c) and (f)). In the middle PTO layer, the rotation direction of the vortex is reversed after the switching events; in the upper and lower PTO layers, they are unchanged. Such rotation switching can change the local chirality and the direction of the toroidal moment [22] once the axial component of polarization is properly controlled. The rotation switching can occur at a length scale of tens of nanometers along the out-of-plane and in-plane directions (Figure S10).

The chirality change kinetics is also revealed by phase-field simulation. The clockwise and counterclockwise vortices shown in Figure 5(a) have mixed axial polarization, in which the overlying red and blue colors denote the directions. Applying an out-of-plane electric field leads to the formation of a uniform c-domain and annihilation of chirality (Figure 5(b)). With the removal of electric fields, the in-plane polarization component ($P_{[010]}$) redistributes concomitant with the gradual recovery of vortex feature (Figure 5(c)-(e)). Such redistribution finally results in the reversal of axial polarization (Figure 5(f)), which can cause chirality switching. Furthermore, during the erasure and recovery process, the vortex positions shift along the in-plane direction, as shown in Figure 5(f), which is also observed experimentally in Figure S11. A chirality flip could occur if the vortex is moved in a one-cell distance (~5 nm) when the clockwise vortex takes the position of its counterclockwise neighbor.

We observed the vortex undergoes a transition from a/c domains to the c domain to accommodate the increasing electric bias and spontaneous recovery with the removal of applied bias. Our atomic-scale evidence supports the previously proposed switching pathways from phase-field simulation [14] but disagrees with the previous experimental studies [16,17]. The previously reported transition from the

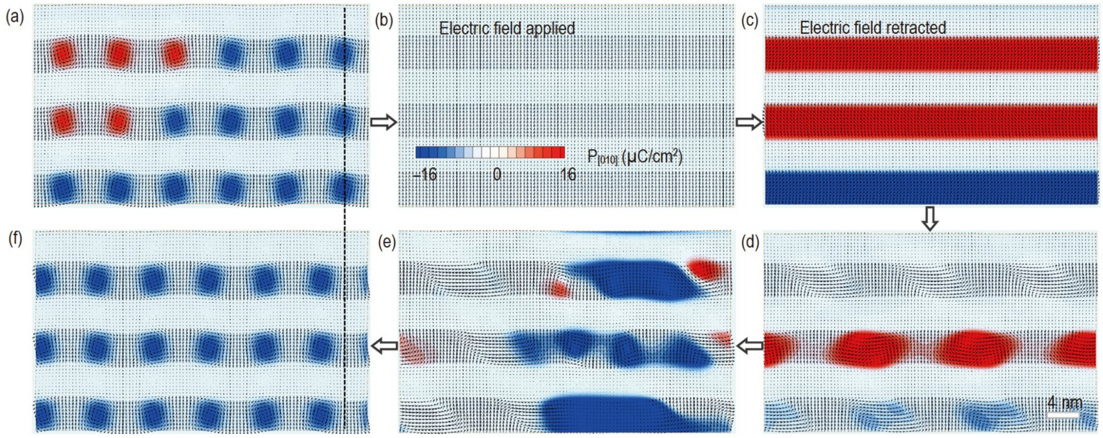

Figure 5 (Color online) Phase-field simulations revealed chirality switching. (a) Pristine vortex array with the blue and red colors indicating the direction of the axial component. Handedness can be determined for individual vortices. (b) Uniform c-domain formed under an out-of-plane electric field of $E_{[001]}$ = 261.2 kV/cm. (c)-(f) Recovery of the vortex with the removal of electric fields. Redistribution of the polarization eventually gives rise to the shift of vortex positions and the reversal of axial polarization, which can alter chirality.

vortex to the polarization wave [16] that is absent in our study may arise from the difference in samples and/or the noncontacting bias mode in their study. Nelson et al. [17] proposed the transition from the vortex to the a/c or a-domain based on the diffraction contrast images. The formation of the a-domain may be caused by the stress during probe contact [18] or the misinterpretation of diffraction contrast images due to the lack of atomic structure. Hong et al. [28] presented the switching between the vortex and the in-plane charged domain under an external electric field in the vortex and a_1/a_2 coexisting system. Nevertheless, the atomic observations presented in our study show that the increasing electric fields break the polar vortex and align the electric dipoles to eventually form the c-domain. The electrically driven switching behavior is also different from that driven by mechanical stress [18]. Prior to the formation of the intermediate a/c domain, the electric field drives the lateral movement of the vortex cores to form the close-pair structure [14], whereas the mechanical stress would not cause any lateral movement before vortex annihilation.

Nevertheless, none of the above work is involved in the rotation reversal or chirality change. The mechanism underlying the change in vortex rotation can be understood as follows. On the one hand, the distributions of strain and static fields are supposed to be uniform laterally once the polarization in the vortex is switched to mono c-domain. Thus, the formation of vortices during the spontaneous back switching has no preference, and the new core positions of the newly generated vortices do not have to be the same as the previous ones. On the other hand, the occurrence of intermediated a/c phase may also give rise to the change in the core positions. As shown in Figure 3(d), the core distance highlighted by the arrow is reduced from 12- to 8-unit cells under an electric field to adapt the realignment of electric dipoles (i.e., the expansion and the shrinkage of upward and downward domains). Previously, the bias-driven lateral movement of the vortex cores has been theoretically predicted to reduce electrostatic energy [14]. In this case, the back switching starting from these intermediate states with either vortex close-pair or a/c domain stripes may not precisely backtrack because of the possible disturbance from random fields [29,33]. Thus, in the end, the rotation of vortices should be different from the original states, leading to chirality change.

Although our simulations and experiments demonstrate that the rotation reversal and position change of vortices are possible, at the current stage, neither the rotation reversal nor position shift can be well controlled because the nucleation of new vortices during the spontaneous back switching can be easily disturbed by the random fields. Precise control of the chirality of a single vortex is possible but requires sophisticated devices. Application of an electric field with out-of-plane (along [001]) and in-plane components (along [010]) can tune the axial polarization to initialize an ordered chirality in the vortex array (Figure S12(a)-(d)). Moreover, single-vortex chirality can be realized through a localized electric bias (Figure S12(e)-(h)). Such a field may be realized in the future through surface probe techniques or patterned with nanosized electrodes from a cross-sectional view. Although four-dimensional STEM [13] can be utilized to characterize the chirality of the topological structures, it may not be compatible with *in situ* equipment because of the relatively large noise or drift environment.

4 Conclusions

In summary, this work reveals the phase transition behavior of individual vortices in $PbTiO_3/SrTiO_3$ superlattices at the atomic scale. The transition starts with vortex core motion and evolves to a/c domains, then to the c-domain with increasing bias. After turning off the bias, the vortex array spontaneously recovers. During the back switching, the rotation of the vortex can be different from the as-grown state, leading to chirality change. The controlled conversion between the topological vortex and the ferroelectric phase may advance the development of nanoelectronic devices with novel functionalities. The demonstrated ability to electrically switch the rotation direction and move the core position of the vortex is one step forward to control chirality by using a simple external electric field and further employing such an order parameter for applications.

This work was supported by the National Natural Science Foundation of China (Grant Nos. 51991340, 51991344, 11974023, 51672007, 21773303, 11875229, and 51872251), the Chinese Academy of Sciences (Grant Nos. XDB33030200, and ZDYZ2015-1), the National Key R&D Program of China (Grant No. 2016YFA0300804), the Key R&D Program of Guangdong Province (Grant Nos. 2018B030327001, 2018B010109009, and 2019B010931001), the Bureau of Industry and Information Technology of Shenzhen (Grant No. 201901161512), the Beijing Excellent Talents Training Support (Grant No. 2017000026833ZK11), and the "2011 Program" Peking-Tsinghua-IOP Collaborative Innovation Center for Quantum Matter.

Supporting Information

The supporting information is available online at phys.scichina.com and http://link.springer.com. The supporting materials are published as submitted, without typesetting or editing. The responsibility for scientific accuracy and content remains entirely with the authors.

1. A. K. Yadav, C. T. Nelson, S. L. Hsu, Z. Hong, J. D. Clarkson, C. M. Schlepütz, C. M. Schlepüetz, A. R. Damodaran, P. Shafer, E. Arenholz, L. R. Dedon, D. Chen, A. Vishwanath, A. M. Minor, L. Q. Chen, J. F. Scott, L. W. Martin, and R. Ramesh, Nature **530**, 198 (2016).
2. R. Ramesh, and D. G. Schlom, Nat. Rev. Mater. **4**, 257 (2019).
3. V. A. Stoica, N. Laanait, C. Dai, Z. Hong, Y. Yuan, Z. Zhang, S. Lei, M. R. McCarter, A. Yadav, A. R. Damodaran, S. Das, G. A. Stone, J. Karapetrova, D. A. Walko, X. Zhang, L. W. Martin, R. Ramesh, L. Q. Chen, H. Wen, V. Gopalan, and J. W. Freeland, Nat. Mater. **18**, 377 (2019).
4. A. K. Yadav, K. X. Nguyen, Z. Hong, P. García-Fernández, P. Aguado-Puente, C. T. Nelson, S. Das, B. Prasad, D. Kwon, S. Cheema, A. I. Khan, C. Hu, J. Íñiguez, J. Junquera, L. Q. Chen, D. A. Muller, R. Ramesh, and S. Salahuddin, Nature **565**, 468 (2019).
5. S. Das, Y. L. Tang, Z. Hong, M. A. P. Gonçalves, M. R. McCarter, C. Klewe, K. X. Nguyen, F. Gómez-Ortiz, P. Shafer, E. Arenholz, V. A. Stoica, S. L. Hsu, B. Wang, C. Ophus, J. F. Liu, C. T. Nelson, S. Saremi, B. Prasad, A. B. Mei, D. G. Schlom, J. Íñiguez, P. García-Fernández, D. A. Muller, L. Q. Chen, J. Junquera, L. W. Martin, and R. Ramesh, Nature **568**, 368 (2019).
6. A. R. Damodaran, J. D. Clarkson, Z. Hong, H. Liu, A. K. Yadav, C. T. Nelson, S. L. Hsu, M. R. McCarter, K. D. Park, V. Kravtsov, A. Farhan, Y. Dong, Z. Cai, H. Zhou, P. Aguado-Puente, P. García-Fernández, J. Íñiguez, J. Junquera, A. Scholl, M. B. Raschke, L. Q. Chen, D. D. Fong, R. Ramesh, and L. W. Martin, Nat. Mater. **16**, 1003 (2017).
7. J. Kim, M. You, K. E. Kim, K. Chu, and C. H. Yang, npj Quantum Mater. **4**, 29 (2019).
8. I. I. Naumov, L. Bellaiche, and H. Fu, Nature **432**, 737 (2004).
9. N. Balke, B. Winchester, W. Ren, Y. H. Chu, A. N. Morozovska, E. A. Eliseev, M. Huijben, R. K. Vasudevan, P. Maksymovych, J. Britson, S. Jesse, I. Kornev, R. Ramesh, L. Bellaiche, L. Q. Chen, and S. V. Kalinin, Nat. Phys. **8**, 81 (2011).
10. Y. L. Tang, Y. L. Zhu, X. L. Ma, A. Y. Borisevich, A. N. Morozovska, E. A. Eliseev, W. Y. Wang, Y. J. Wang, Y. B. Xu, Z. D. Zhang, and S. J. Pennycook, Science **348**, 547 (2015).
11. P. Sharma, Q. Zhang, D. Sando, C. H. Lei, Y. Liu, J. Li, V. Nagarajan, and J. Seidel, Sci. Adv. **3**, e1700512 (2017).
12. P. Shafer, P. García-Fernández, P. Aguado-Puente, A. R. Damodaran, A. K. Yadav, C. T. Nelson, S. L. Hsu, J. C. Wojdeł, J. Íñiguez, L. W. Martin, E. Arenholz, J. Junquera, and R. Ramesh, Proc. Natl. Acad. Sci. USA **115**, 915 (2018).
13. P. Behera, M. A. May, F. Gpmez, S. Susarla, and S. Das, arXiv: 2105.14109.
14. Z. Hong, and L. Q. Chen, Acta Mater. **152**, 155 (2018), arXiv: 1711.00995.
15. L. L. Ma, Y. Ji, W. J. Chen, J. Y. Liu, Y. L. Liu, B. Wang, and Y. Zheng, Acta Mater. **158**, 23 (2018).
16. K. Du, M. Zhang, C. Dai, Z. N. Zhou, Y. W. Xie, Z. H. Ren, H. Tian, L. Q. Chen, G. Van Tendeloo, and Z. Zhang, Nat. Commun. **10**, 4864 (2019).
17. C. T. Nelson, Z. Hong, C. Zhang, A. K. Yadav, S. Das, S. L. Hsu, M. Chi, P. D. Rack, L. Q. Chen, L. W. Martin, and R. Ramesh, Microsc. Microanal. **25**, 1844 (2019).
18. P. Chen, X. Zhong, J. A. Zorn, M. Li, Y. Sun, A. Y. Abid, C. Ren, Y. Li, X. Li, X. Ma, J. Wang, K. Liu, Z. Xu, C. Tan, L. Chen, P. Gao, and X. Bai, Nat. Commun. **11**, 1840 (2020), arXiv: 1910.00182.
19. I. I. Naumov, and H. Fu, Phys. Rev. Lett. **101**, 197601 (2008), arXiv: 0808.2832.
20. J. Wang, and M. Kamlah, Phys. Rev. B **80**, 012101 (2009).
21. S. Prosandeev, I. Ponomareva, I. Kornev, and L. Bellaiche, Phys. Rev. Lett. **100**, 047201 (2008).
22. L. Van Lich, T. Shimada, J. Wang, V. H. Dinh, T. Q. Bui, and T. Kitamura, Phys. Rev. B **96**, 134119 (2017).
23. S. Yuan, W. J. Chen, L. L. Ma, Y. Ji, W. M. Xiong, J. Y. Liu, Y. L. Liu, B. Wang, and Y. Zheng, Acta Mater. **148**, 330 (2018).
24. A. Y. Abid, Y. Sun, X. Hou, C. Tan, X. Zhong, R. Zhu, H. Chen, K. Qu, Y. Li, M. Wu, J. Zhang, J. Wang, K. Liu, X. Bai, D. Yu, X. Ouyang, J. Wang, J. Li, and P. Gao, Nat. Commun. **12**, 2054 (2021).
25. L. Lu, Y. Nahas, M. Liu, H. Du, Z. Jiang, S. Ren, D. Wang, L. Jin, S. Prokhorenko, C. L. Jia, and L. Bellaiche, Phys. Rev. Lett. **120**, 177601 (2018).
26. X. Li, C. Tan, C. Liu, P. Gao, Y. Sun, P. Chen, M. Li, L. Liao, R. Zhu, J. Wang, Y. Zhao, L. Wang, Z. Xu, K. Liu, X. Zhong, J. Wang, and X. Bai, Proc. Natl. Acad. Sci. USA **117**, 18954 (2020), arXiv: 1911.09822.
27. Y. Sun, A. Y. Abid, C. Tan, C. Ren, M. Li, N. Li, P. Chen, Y. Li, J. Zhang, X. Zhong, J. Wang, M. Liao, K. Liu, X. Bai, Y. Zhou, D. Yu, and P. Gao, Sci. Adv. **5**, eaav4355 (2019).
28. Z. Hong, S. Das, C. Nelson, A. Yadav, Y. Wu, J. Junquera, L. Q. Chen, L. W. Martin, and R. Ramesh, Nano Lett. **21**, 3533 (2021).
29. P. Gao, C. T. Nelson, J. R. Jokisaari, S. H. Baek, C. W. Bark, Y. Zhang, E. Wang, D. G. Schlom, C. B. Eom, and X. Pan, Nat. Commun. **2**, 591 (2011).
30. X. Z. Yu, Y. Onose, N. Kanazawa, J. H. Park, J. H. Han, Y. Matsui, N. Nagaosa, and Y. Tokura, Nature **465**, 901 (2010).
31. N. Romming, C. Hanneken, M. Menzel, J. E. Bickel, B. Wolter, K. von Bergmann, A. Kubetzka, and R. Wiesendanger, Science **341**, 636 (2013).
32. W. Jiang, P. Upadhyaya, W. Zhang, G. Yu, M. B. Jungfleisch, F. Y. Fradin, J. E. Pearson, Y. Tserkovnyak, K. L. Wang, O. Heinonen, S. G. E. te Velthuis, and A. Hoffmann, Science **349**, 283 (2015), arXiv: 1502.08028.
33. S. Jesse, B. J. Rodriguez, S. Choudhury, A. P. Baddorf, I. Vrejoiu, D. Hesse, M. Alexe, E. A. Eliseev, A. N. Morozovska, J. Zhang, L. Q. Chen, and S. V. Kalinin, Nat. Mater. **7**, 209 (2008).